

Characterization of as-cast microstructural heterogeneities and damage mechanisms in eutectic AlCoCrFeNi_{2.1} high entropy alloy



Deep Choudhuri^{a,b,*¹}, Shivakant Shukla^a, Philip A. Jannotti^c, Saideep Muskeri^a, Sundeep Mukherjee^{a,b}, Jeffrey T. Lloyd^c, Rajiv S. Mishra^{a,b}

^a Department of Materials Science and Engineering, University of North Texas, Denton, TX, 76207, USA

^b Advanced Materials and Manufacturing Processes Institute, University of North Texas, Denton, TX, 76207, USA

^c US Army Research Laboratory, Aberdeen Proving Ground, MD, 21005, USA

ARTICLE INFO

Keywords:

High entropy alloy
Deformation
TEM
EBSD
Crystallography

ABSTRACT

We have correlated as-cast microstructural features of AlCoCrFeNi_{2.1} with adiabatic shear localization (ASL) and crack formation, due to dynamic deformation from impact with a spherical projectile. The as-cast microstructure contained extensive FCC/B2 Kurdjumov-Sachs interfaces, and the BCC-ordered B2 domains had plate-like lamellae and clusters of irregularly-shaped morphologies. The primary FCC and B2 phases also contained FCC-ordered L₁₂ and Cr-rich precipitates, respectively. ASL propagated across all FCC/B2 interfaces, and the varying B2 morphologies did not hinder its formation. ASL propagation involved subgrain formation and nanoscale-twinning inside FCC, while the B2 domains experienced extensive dislocation plasticity, even though the impact velocities and B2 morphologies influenced crack formation discernibly. At lower impact velocities the lamellar B2 regions were prone to crack propagation along the FCC/B2 interfaces. In comparison, at higher impact velocities, the cracks traced the locus of ASL paths; i.e., cracks propagated through lamellar and irregularly-shaped B2 domains alike. Deformation-induced steps formed at the FCC/B2 interfaces may have facilitated such trans-domain morphology-agnostic crack propagation. Finally, L₁₂ precipitates minimally impacted any damage mechanisms, while Cr-rich precipitates deflected crack paths inside the B2 domains. Thus, efforts to engineer eutectic high entropy alloy microstructures should strengthen FCC/B2 interfaces in the lamellar regions while retaining the strengthening Cr-rich precipitates.

1. Introduction

High entropy alloys (HEAs) have received recent, significant attention as a promising class of materials for structural applications [1–6]. HEAs offer the flexibility to select elemental combinations over a large composition space, which, in principle, allows us to tailor strength, ductility and work-hardenability for load-bearing applications [4–6]. Accordingly, over the years, the search for better mechanical properties has transitioned HEA composition foci from those with equiatomic concentrations, e.g., CoCrFeMnNi; towards compositions containing multi-principal elements forming multiple phases, e.g., Al_xCoCrFeNi ($x = 0.1, 0.3, 0.5$) [1–12]. Such a trend also mirrors the transition in desired HEA microstructures, i.e., from single-phase, solid-solution to microstructures containing secondary phases of varying volume fractions [4–12].

In keeping with those notions, eutectic alloy compositions

containing FCC-B2 phases were developed recently as a new sub-class in the HEA family — a sub-class hereinafter called eutectic high entropy alloys or EHEAs [13–29]. Examples of prominent FCC-B2 EHEAs include Fe₃₀Ni₂₀Mn₃₅Al₁₅ [13,14], Al_{0.7}CoCrFeNi [15–20] and AlCoCrFeNi_{2.1} [21–29]. However, among the three EHEA compositions, Al_{0.7}CoCrFeNi and AlCoCrFeNi_{2.1} appear to exhibit better mechanical properties, particularly tensile ductility [13,14,20–22,28]. Both Al_{0.7}CoCrFeNi and AlCoCrFeNi_{2.1} also exhibit similar kinds of secondary phases in the primary FCC and B2 constituents [15–29]. Recent deformation studies on Al_{0.7}CoCrFeNi have demonstrated that FCC-ordered L₁₂ precipitates in the FCC phase increase its flow strength in both quasistatic and high strain-rate conditions involving split-Hopkinson pressure bar [19,20]. Furthermore, nanoindentation experiments performed on Al_{0.7}CoCrFeNi suggested that B2 can transform to FCC [17]; meaning complex stress states, e.g., under the indenter tip, can trigger such transformations. On the other hand, AlCoCrFeNi_{2.1} has

* Corresponding author. ;Department of Materials Science and Engineering, University of North Texas, Denton, TX, 76207, USA.
E-mail address: deep.choudhuri@unt.edu (D. Choudhuri).

¹ Present address: Department of Materials and Metallurgical Engineering, New Mexico Institute of Mining and Technology, Socorro, NM, 87801, USA.

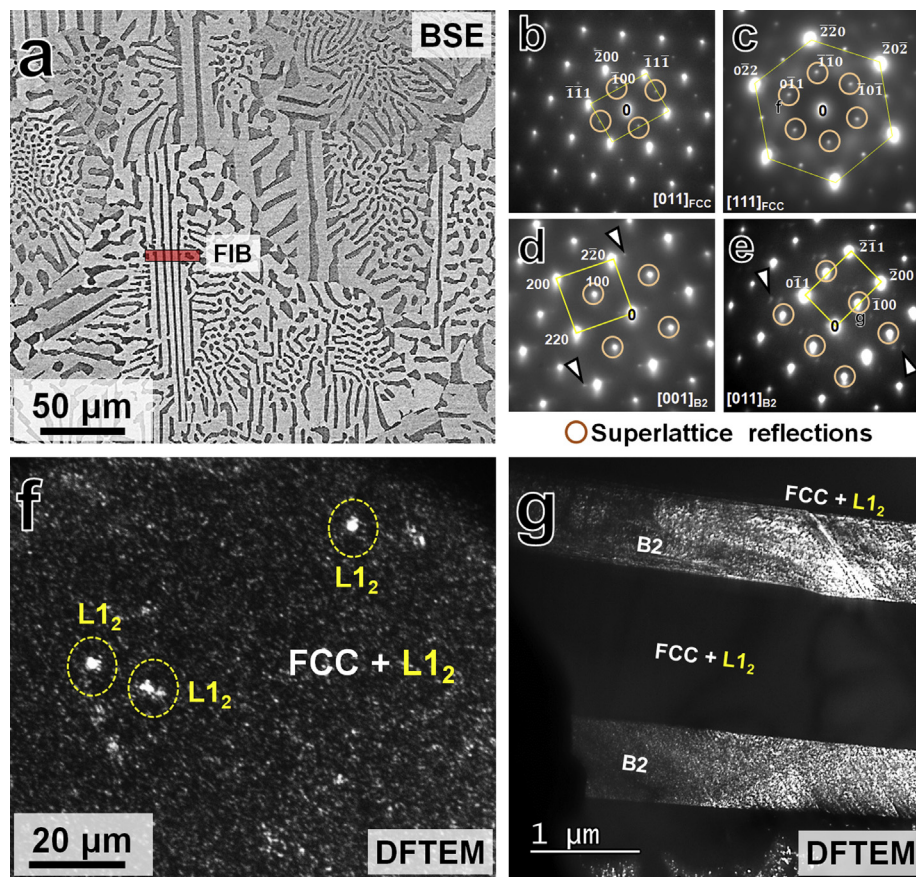


Fig. 1. (a) Back-scattered SEM (BSE) of the as-cast EHEA microstructure, where the darker and lighter contrast regions are the FCC and B2 phases. Inset shows precipitates within the darker B2 phase. TEM of the EHEA microstructure: selected area diffraction patterns (SADPs) showing (b) [011] and (c) [111] zone axes form the FCC phase, (d) [001] and (e) [011] zone axes of B2, and dark-field TEM images showing (f) L1₂ precipitation inside FCC phase and (g) plate-like lamellar B2.

been examined widely; and has included its castability, phase identification, tensile ductility, compression responses, dislocation mechanisms and microstructure under severe plastic deformation [21–27]. Deformation studies conducted on AlCoCrFeNi_{2.1} have confirmed that the B2 phase exhibits substantial dislocation activity [28] and does not disorder or undergo phase transformation during severe plastic deformation [23–27]. Interestingly, Al_{0.7}CoCrFeNi manifests nanoscale twins in the FCC phase during quasistatic testing, while AlCoCrFeNi_{2.1} does not [20,28]. Therefore, likely AlCoCrFeNi_{2.1} will manifest FCC-twinning at higher strain rates, since the twinning in FCC-HEAs occurs at conditions involving high flow stresses.

In this study we examined the deformed microstructure of AlCoCrFeNi_{2.1} EHEA that has been impacted with Tungsten-Carbide (WC) spherical projectiles launched at different velocities; i.e., ballistic testing of EHEA. Impact with a spherical projectile is a type of high strain-rate loading that is believed to produce a spherical shock front followed by deformation due to projectile penetration into the target material [30]. These conditions expose the materials to extreme conditions involving very high temperatures and local strains reaching up to ~500% [30]. The primary deformation/damage mechanism in this case is called adiabatic shear-strain localization [31,32]. Such localization results in local regions where plastic flow is concentrated in a networked pattern, as compared to adjacent regions that can experience little deformation. In essence, adiabatic shear localization or band formation is a competition between strain-hardenability and thermal softening, meaning higher strain-hardenability will resist failure via adiabatic shear localization [31,32].

A key aspect of FCC-B2 EHEAs is that their microstructures are dominated by interphase FCC/B2 interfaces (other than grain boundaries) [13–29]. Therefore, during plastic deformation, unit mechanisms, e.g., dislocation, stacking faults, twins, and the like, are bound to interact with such FCC/B2 interfaces [20,28,29]. It is likely that FCC/B2 interfaces may prevent adiabatic shear localization, because

interaction of the shear front with the hard intermetallic B2 phase is expected to interrupt the “run away” plastic flow occurring in the softer FCC regions. Consequently, such interfaces are expected to dominate the plasticity and damage of these materials. These considerations mandate a systematic examination of the EHEA microstructure; e.g., the crystallographic relationship between FCC and B2, and precipitation in both phases, because information from such characterization efforts will permit us to correlate deformation and damage mechanisms to the pre-existing microstructural heterogeneities. Therefore, we have examined the as-cast microstructure of AlCoCrFeNi_{2.1} systematically, and have correlated the heterogeneities in as-cast microstructures with the formation and propagation of adiabatic shear localization and crack formation.

2. Experimental details

As-cast alloy of composition AlCoCrFeNi_{2.1} (in atomic ratio) was obtained from Sophisticated Alloys as 203 × 102 × 102 mm, 8 × 4 × 4 in, (length × height × width) ingots. Target plates with nominal dimensions 102 × 102 × 12.7 mm, or 0.5 × 4 × 4 in, were cut from as-cast ingots. Terminal ballistic testing was conducted at the U.S. Army Research Laboratory (Aberdeen Proving Ground, MD, USA). The plates were impacted with WC spherical (radius 6.35 mm or 0.25") projectiles at velocities of 803, 1159, and 1388 m/s. Description of the ballistic testing procedure is provided elsewhere [30–33]. Microstructural characterization on pre- and post-deformation specimens was performed using FEI's NovaNano SEM230 scanning electron microscope (SEM) and Tecnai G2 F20 ST S/TEM transmission electron microscope (TEM) operating at 200 kV. The SEM was equipped with a Hikari Super™ EBSD detector that allowed us to vary step size from 0.04–0.5 μm and to capture high-resolution electron backscattered diffraction (EBSD) datasets. The TEM was outfitted with liquid nitrogen-cooled EDAX™ windowless silicon drift detector (Model Optima-

T-30) with an active area of 300 mm sq. and solid angles up to 0.5 steradian. The setup permitted energy dispersive spectroscopy (EDS) over large areas in scanning transmission electron microscopy (STEM) mode. Site-specific TEM foils were prepared in FEI's dual-beam Nova 200 NanoLab FIB/SEM. Mechanical responses of the as-case microstructure was also examined via quasi-static tensile (strain rate $\sim 10^{-3}$ s $^{-1}$) and high strain rate split-Hopkinson pressure bar (strain rate $\sim 10^3$ s $^{-1}$) tests. Experimental details of quasistatic and SHPB testing are described in Refs. [9,10,19,20], respectively.

3. Results

3.1. Initial microstructure: phase analysis and crystallography

A backscattered secondary electron (BSE) micrograph presented in Fig. 1 (a) shows the microstructure of the EHEA in the as-cast condition. The BSE regions of darker and brighter contrast indicated that at this scale the EHEA is comprised nominally of two phases. Literature reports suggest that the bright and dark contrasts correspond to FCC and B2 phases, respectively [21–29]. To confirm the presence of both phases, a TEM foil was extracted using focused ion beam (FIB) from the as-cast microstructure containing lamellar features (Fig. 1 (a)). Selected area diffraction patterns (SADPs) recorded from two zone axes (ZAs) of both phases are presented in Fig. 1 (b)–(e). The FCC phase was revealed from

the symmetry of the [011]_{fcc} and [111]_{fcc} ZA SADPs (Fig. 2 (b) and Fig. 2 (c)). These ZAs also contained additional low-intensity {001} and {110} superlattice reflections (circled in Fig. 1 (b) and 1 (c)), which indicated the presence of FCC-ordered L1₂ phase within the FCC matrix. On the other hand, the ZAs presented in Fig. 2 (d) and 2 (e) resembled [001]_{bcc} and [011]_{bcc} of BCC, respectively, and also contained {001} superlattice reflections corresponding to BCC-ordered B2 phase (superlattices are circled in the SADPs).

The distribution and morphology of the ordered phases were also compared via dark-field TEM (DFTEM) imaging, and were recorded by selecting the ordered {001} reflections from the [011]_{bcc/fcc} SADPs. The corresponding DFTEM of L1₂ precipitates and lamellar B2 plates is shown in Fig. 1 (f) and 1 (g), respectively. The L1₂ precipitates were present as clusters (marked with dotted circles in Fig. 1 (f)), while the remaining FCC matrix had a speckled/mottled appearance, which could be due to even finer-scale L1₂ precipitation or perhaps is characteristic of the parent phase. (Such mottling were also observed in the BCC-matrix of metastable beta-stabilized Titanium alloys [34]). The B2 domains also contained additional precipitate phases, which produced additional satellite reflections in [001]_{bcc} and [011]_{bcc} SADPs (marked with arrows in Fig. 1 (d) and 1 (e)). A STEM-EDS based qualitative elemental map from a larger B2 domain revealed that such precipitation was caused by Cr enrichment (Fig. 2). These Cr-rich “spherical” regions were depleted in Ni and Al, while Fe and Co do not exhibit any

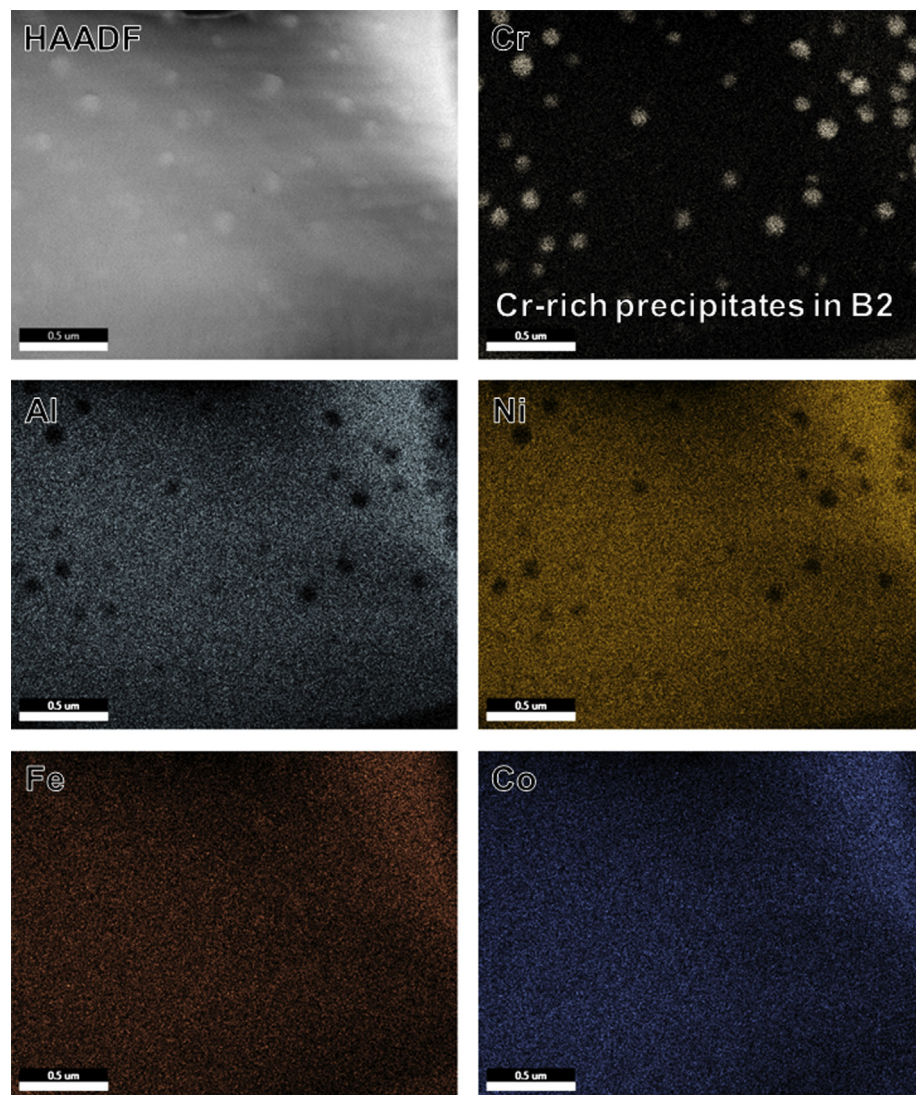


Fig. 2. STEM-EDS-based qualitative elemental mapping inside a B2 domain showing the presence of Cr-rich precipitates.

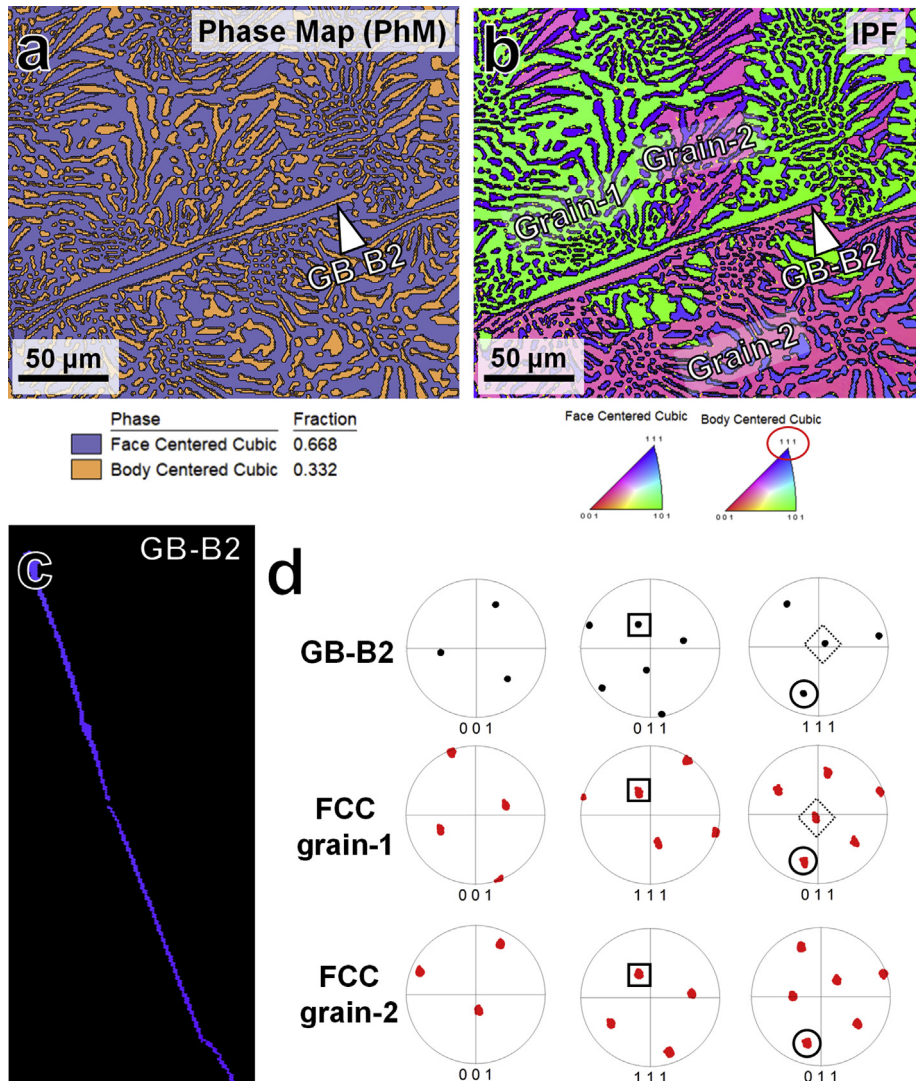


Fig. 3. EBSD of the as-cast EHEA microstructure: (a) phase map, (b) color-coded inverse pole figure (IPF), (c) IPF of an inter-granular grain boundary B2 (GB-B2) shown in (a) and (b), and (d) comparison of {001}, {011} and {111} pole figures of GB-B2 and the neighboring FCC grains. (For interpretation of the references to color in this figure legend, the reader is referred to the Web version of this article.)

discernible change within the B2 matrix. Literature reports suggest the Cr-rich regions may be formed via spinodal decomposition of the B2 phase during solidification [28,35], and may explain the presence of satellite reflections in the SADPs in Fig. 1 (d) and 1 (e)). Hereon, we will only focus on the constituents present in the as-cast microstructure because they are of direct relevance to its mechanical response. A detailed examination of the formation mechanism/s associated with EHEA as-cast microstructure is currently under progress. Notwithstanding, taken together, our TEM results reveal a complex as-cast EHEA microstructure, where the primary eutectic FCC and B2 products undergo secondary solid-state decomposition processes, i.e., L1₂ and Cr-enrichment.

A careful examination of the as-cast microstructure also confirms that the B2 domain acquires a variety of morphologies (Fig. 1 (a)), i.e., lamellar to irregularly-shaped. Therefore, at this micron length scale, we examined the B2 distributions and their crystallography in detail by using EBSD-based techniques. Fig. 3 (a) and 3 (b) show the phase map (indicated as PhM in Fig. 3 (a)) and the pseudo-colored inverse pole figure (or IPF), respectively, which was acquired at the junction of two FCC grains. Color coding for the phase map and IPF is also shown below each panel. In particular, below the IPF in Fig. 1 (b), we used circles to identify the approximated orientations of FCC and B2 phases in their

respective pseudo-colored stereographic triangles. The same convention was followed wherever stereographic triangles are shown. As expected, the phase map revealed a very high fraction of B2 (~33%) in the microstructure (Fig. 3 (a)). The IPF also confirmed that the EHEA microstructure contained interpenetrating FCC grains, which are marked as Grain-1 (close to $a < 001 >_{\text{fcc}}$) and Grain-2 (close to $a < 011 >_{\text{fcc}}$) in Fig. 3 (b). Interestingly, within the area scanned, all the B2 domains were aligned along one of the $< 111 >_{\text{bcc}}$ (see BCC IPF at the bottom of Fig. 3 (b)). Such similarly oriented groups of B2 domains, with common orientations along different BCC crystallographic axes (other than $[111]_{\text{bcc}}$), were observed throughout the EHEA microstructure, and likely are characteristic features of eutectic HEAs.

The FCC-B2 crystallographic relationship was investigated by separating the B2 domains into those lying at the grain boundaries (hereafter GB-B2) and intragranular regions. Fig. 3 (c) shows a highlighted IPF of a GB-B2 (also marked with arrows in Fig. 3 (a) and 3 (b)), while Fig. 3 (d) depicts the {001}, {011} and {111} pole figures extracted from the same GB-B2 (top panel) and pole figures (bottom two panels) from its two adjoining FCC grains (Grain-1 and Grain-2 in Fig. 3 (b)). The common poles from the three microstructural entities, indicated with bold circles and square symbols in Fig. 3 (d), reveal that the GB-B2 shares a Kurdjumov-Sachs (KS) orientation relationship (OR)

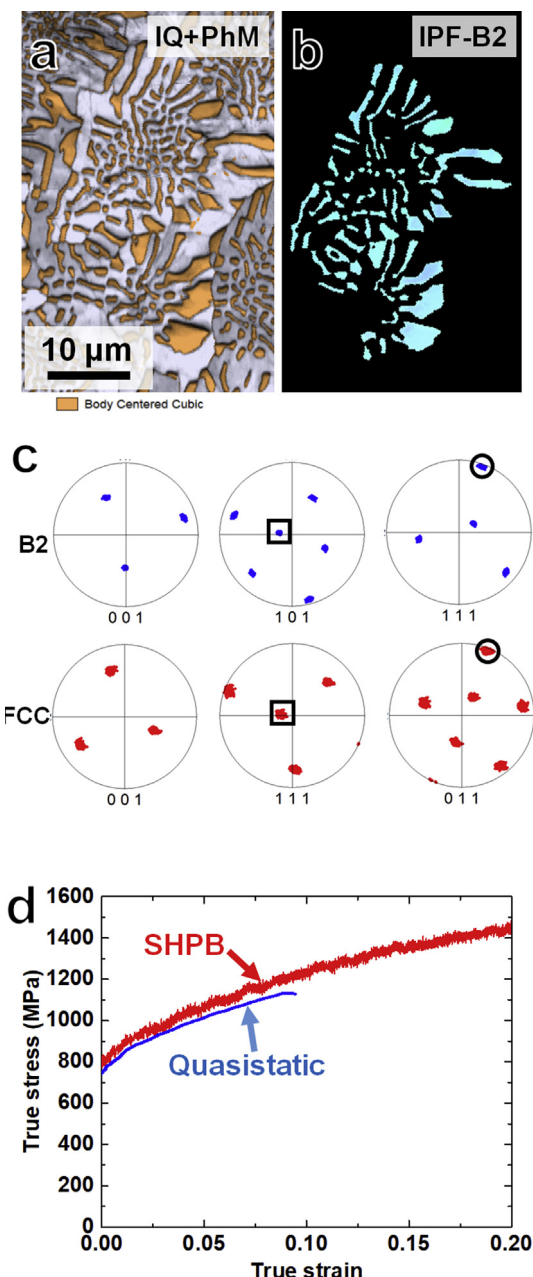


Fig. 4. EBSD based crystallography of irregularly-shaped B2 domains: (a) phase map, (b) IPF highlighting the lamellar B2, and (c) comparison of {001}, {011} and {111} pole figures of the B2 clusters and the parent FCC grain. (d) Comparison of mechanical responses under quasi-static and high strain-rate conditions.

with both FCC grains; i.e., $<011>_{B2} // <111>_{FCC}$ and $\{111\}_{B2} // \{011\}_{FCC}$ [43,44]. Interestingly, the $\{111\}_{B2}$ pole of GB-B2 is nearly parallel to the $\{011\}_{FCC}$ of its neighboring Grain-1, which is marked with a dotted diamond symbol in Fig. 3 (d). This extra crystallographic alignment between GB-B2 and Grain-1 suggests that the GB-B2/Grain-1 interface might be “stronger” compared to GB-B2/Grain-2. Likely the geometrical constraints imposed by such extra crystallographic alignment may impact the local plastic deformation in the regions surrounding GB-B2s.

Fig. 4 (a) shows the phase map (overlaid with image quality or IQ) of intragranular B2 domains, where the irregularly-shaped B2s are arranged in cluster; while Fig. 4 (b) shows the IPF from a selected B2 cluster. We emphasize that in this cluster, each B2 domain is oriented in the same crystallography direction (i.e., the same pseudo color coding).

{001}, {011} and {111} pole figure plots extracted from the selected B2 cluster and the parent FCC grain are presented in Fig. 4 (c). Comparison of the pole figures indicated the KS OR between the two phases. (Though not presented here, the lamellar B2 grains also shared KS OR with FCC [36]). However, unlike the GB-B2 (i.e., Fig. 3 (d)), none of the B2 domains shared an extra crystallographic pole with their host FCC grain. For completion, the mechanical responses of EHEA under low (quasi-static) and high (SHPB) strain rates was also compared (Fig. 4d). We find that the material exhibits good ductility (strain to failure (ϵ_f) $\sim 11\%$) and the flow stress remains largely unaffected by the strain rate. These results suggest that the operative deformation mechanisms remains largely similar between 10^{-3} and 10^{+3} 1/s. A TEM based study of EHEA deformation at various strain-rates is currently in progress [36].

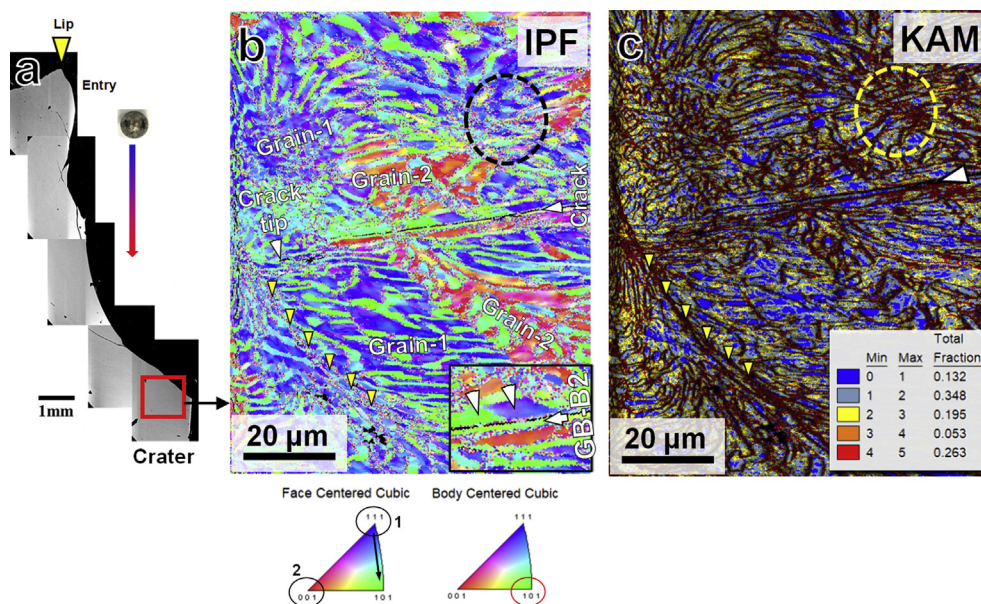
Next, we examined the influence of the above-mentioned structural and crystallographic features on the damage caused by adiabatic shear localization in ballistically loading as-cast EHEA. Three ballistically-loaded conditions were examined, and, based on literature nomenclature [30–32], can be categorized as follows:

1. Partial penetration — after impact with the EHEA plate, the projectile travels through the material before stopping (section 3.2.1);
2. Plug formation — at higher projectile velocity, the impact produces additional protrusion on the backside of the plate (section 3.2.2); and
3. Full or complete penetration — at still higher projectile velocities, the projectile completely travels through the material without stopping (section 3.2.3)

3.1.1. Deformation features in the partially penetrated condition

Fig. 5 (a) shows the macroscopic surface manifestation of failure features in the partially penetrated path via a montage of SEM images recorded from the regions next to the projectile penetration path. The surface manifestation of adiabatic shear localization and the corresponding crack formation were examined in detail using EBSD. Fig. 5 (b) shows the IPF (along with the pseudo-colored stereographic maps for the FCC and BCC (or B2) regions at the bottom of Fig. 5 (b)); and Fig. 5 (c) depicts the corresponding Kernel average misorientation (KAM). The IPF in Fig. 5 (b) reveals very fine cracks located between two grains, which are marked as “Grain-1” and “Grain-2” and are oriented nominally close to {001} and {111}, respectively. (See stereographic maps below.) Closer inspection of the failed region confirmed that the crack propagated along GB-B2 (marked with arrows in the inset of Fig. 5 (b)), and that the Grain-1 FCC region, next to the crack, had undergone large lattice distortion (marked by arrows in the inset of Fig. 5 (b)). The crystallographic reorientation corresponding to such distortion is indicated with an arrow in the FCC pseudo-colored stereographic maps, which show that locally the lattices have rotated from {111} to {101} orientations. The large lattice reorientation near the cracked region could have resulted from the preexisting geometric constraints imposed by the extra common orientation between the GB-B2 and its neighboring FCC grain (Fig. 3 (d)). Such constraints may have forced the neighboring FCC grain (without the extra common orientation) to undergo lattice reorientation as a means of relieving built-up local stresses. Nonetheless, our EBSD results indicate that intergranular B2s are a potent cause of failure, because they permit crack propagation along their length, i.e., interfacial decohesion.

Additionally, shear bands were also noted in the IPF (Fig. 5 (b)) and the corresponding KAM (Fig. 5 (c)), where an array of yellow-colored arrow heads nominally indicates locus of the shear bands. Note that shear localization being almost unaffected by the individual B2 domains suggested that the region may have lost strength by local “softening” via adiabatic shear localization (ASL) [30–32]. The severity of the plastic deformation within and around ASL was confirmed via KAM map (marked with arrows in Fig. 5 (c)), and typically is used to show geometrically necessary dislocations in a given region [27,29]. The



KAM further revealed dislocation density near the FCC/B2 interfaces, and that the cluster of irregularly-shaped B2 domains (dotted ellipse in Fig. 5 (b) and 5 (c)) indicated that such interfaces are crucial for accommodating plastic deformation.

We further examined the region near the tip of the interfacial crack propagating along the GB-B2 (Fig. 5 (b)). Fig. 6 (a) is a BSE of the crack tip region, which shows that crack trajectory had deviated at two locations — arrows “1” and “2”. The first deviation occurs when the crack transitions from an intergranular FCC/GB-B2 interface to an intragranular FCC/B2 interface (which is a part of the intragranular lamellar domain inside Grain-1 in Fig. 5 (b)). The second deviation occurs when the crack encounters an ASL (marked with yellow-colored arrow heads), and its trajectory shifts to another FCC/B2 interface within the same lamellar domain. Worth emphasizing is that, irrespective of the deviation, the crack path was maintained invariably along the FCC/B2 interface. Therefore, the FCC/B2 within the intragranular plate-like B2 lamellar domains, much like the GB-B2 (Fig. 5 (b)), are likely sources of failure in EHEAs.

To gain additional insight into deviation of crack path from inter-to intragranular FCC/GB-B2 interfaces (arrow “1” in Fig. 6 (a)), high-resolution EBSD was performed using step size of 80 nm on the lamellar B2 domains (dotted rectangle in Fig. 6 (a)). Fig. 6 (b1) and 6 (b2) show the corresponding phase and IPF maps of the B2 lamellae containing the crack, respectively. These high-resolution EBSD results further allowed us to extract pole figures from the B2 region near the crack and neighboring FCC regions (marked as “FCC-B”(bottom) and “FCC-T”(top)). The {001}, {011} and {111} pole figures presented in Fig. 6 (c) indicated that, although the FCC/B2 KS OR is maintained (marked by squares and circles), the B2, FCC-B and FCC-T regions shared extra common poles or orientations, e.g., (001) pole marked with a triangle. Note that such a common pole between the parent FCC grain and B2 domains did not exist in the as-cast microstructure (Figs. 3 (d) and 4 (c)). Consequently, a reasonable assumption is that the common pole was caused by the ballistic loading process. Furthermore, the specific (001) orientation may have been caused by the constraining influence of the neighboring Grain-2 (Fig. 5 (b)) whose average orientation was close to (001). Regardless, the deviation in crack trajectory appears to have been meant to relieve the local buildup of local stresses caused by lattice reorientation. More importantly, EBSD results presented in Figs. 5 and 6 reveal that the FCC regions near the plate-like B2 domains (irrespective of inter- or intragranular) are most susceptible to significant lattice reorientations during severe plastic deformation.

Fig. 5. (a) SEM montage of projectile path in the partially penetrate condition. EBSD of a region outlined with a box in (a); (b) IPF of the entire region, where the inset shows a local variation in FCC orientation near a FCC/B2 interfacial crack, and (c) Kernel average misorientation (KAM) map of the same region. The yellow colored arrows in (b), and (c) mark the path of adiabatic shear localization (ASL). (For interpretation of the references to color in this figure legend, the reader is referred to the Web version of this article.)

3.1.2. Deformation features in the plugged condition

The BSE image presented in Fig. 7 (a1) reveals that shear localization was even more pronounced in the plugged condition. Fig. 7 (a1) shows the specific location near the projectile penetration path. Also, in Fig. 7 (a1) is the ASL path, as indicated with an array of yellow-colored arrow heads. The ASL had traversed through both irregularly-shaped B2 clusters and the B2 lamellae alike. A closer inspection of the ASL path (dotted rectangle in Fig. 7 (a1) and shown in Fig. 7 (b)) revealed ellipsoidal micro-cracks within FCC and B2 phases. Interestingly, the crack within the irregularly-shaped B2 domain exhibited a zig-zag trajectory (inset in Fig. 7 (b)), and such tortuosity may have been caused by the pre-existing Cr-rich regions within which the crack may have deflected (Fig. 2).

Furthermore, EBSD performed on the dotted region in Fig. 7 (a1) provided additional evidence of ASL via the IPF (Fig. 7 (c)) and phase (Fig. 7 (d)) maps (image quality overlaid on both), where the ASL was clearly observed to shear one of the irregular B2 domains (white arrows in Fig. 7 (b)-(d)). To better understand the deformation features near the ASL (since regions with ASL could not be indexed using EBSD), we carried out a higher-resolution EBSD scan of a region near the ASL (white rectangle in Fig. 7 (d)) by using step size of 40 nm. The corresponding IPF map (Fig. 7 (e)) showed signature of extensive damage within the B2 domains, since those regions could not be indexed (white arrows in Fig. 7 (e)). Interestingly, even at such small EBSD step size, deformation twinning within the FCC regions could not be resolved. This is surprising, because twinning in FCC-based metals and HEAs typically is accentuated under high strain-rate conditions [37,38]. However, the IPF in Fig. 7 (e) does not preclude the presence of nano-scale twins (typically seen in FCC-based HEAs [39,40]), which are not resolvable by traditional EBSD techniques used here.

3.1.3. Deformation features in the fully penetrated condition

Surface manifestation in the fully penetrated specimens is depicted in Fig. 8 (a) (also see inset in lower right-hand corner). The damage features were markedly different from the partially penetrated and plugged conditions via the presence of distinct “V”-shaped crack (compare Figs. 5 (a) and 7 (a2)). A higher magnification BSE image of the “V”-shaped crack (Fig. 8 (a)) shows that the angle between the “V”-shaped cracks varied between ~45 and 54°. Such surface manifestation are comparable to slip-line formed during indentations [32]. The region between the two “V”-shaped cracks as further examined (red rectangle and marked “b” in Fig. 8 (a)) in higher magnification (Fig. 8 (b))

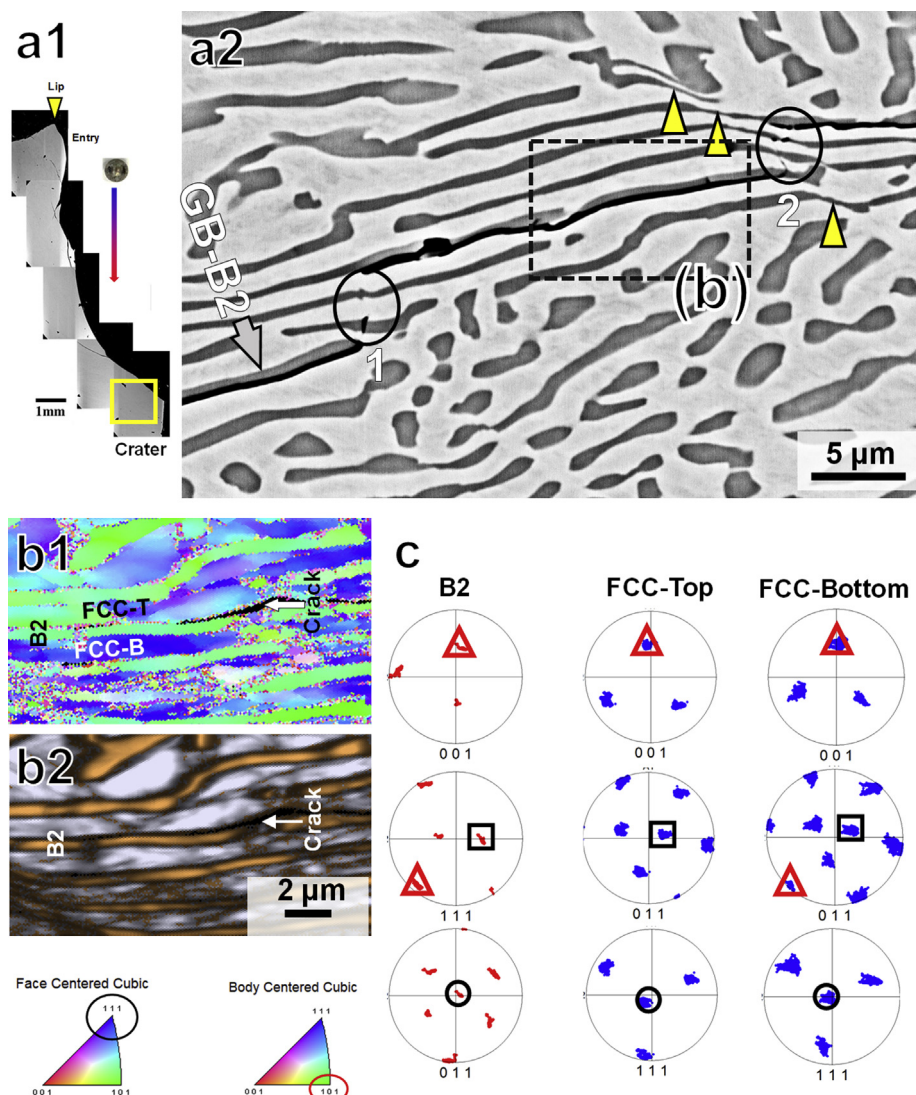


Fig. 6. (a1) SEM montage of projectile path in the partially penetrate condition and (a2) is a higher magnification BSE of the crack tip showing deviations in the trajectory of the FCC/B2 interfacial crack. (b) EBSD showing a lamellar B2 region which is also outlined with a box in (a): (b1) IPF showing a crack along FCC/B2 and (b2) the corresponding phase map overlaid with IQ. Here, the adjoining FCC regions on the top (FCC-T) and bottom (FCC-B) of B2. (c) comparison of {001}, {011} and {111} pole figures of the B2 plate, and the top and bottom FCC regions.

exhibited extensive ALS formation (four different arrays of colored arrowheads in Fig. 8 (b)). “Blunt” near-ellipsoidal cracks were in one of the ASL paths (red-colored arrows in Fig. 8 (b)). Such cracks are believed to have formed inside the shear localization zones via void nucleation and subsequent coalescence [31,32,41,42]. Traces of such voids are also seen along the ASL path indicated with blue colored arrows. The ASLs had sheared through both the plate-like lamellar B2 (Fig. 8 (c)) and had even intersected a coarser B2 with irregular morphology (Fig. 8 (d)). Therefore, consistent with previous observations on the partially penetrated and plugged condition specimens, the ASLs have sheared through the B2 domains irrespective of their shape and distribution; and “extent” of B2 shearing appears to be more pronounced compared to the other conditions. Finally, note that, unlike the partially penetrated and plugged specimens, in the fully penetrated condition, crack propagation along FCC/B2 interfaces was indiscernible from BSE images.

To understand the influence of ASL propagation on the FCC and B2 phases, we also extracted site-specific TEM foils via FIB from locations marked in Fig. 8 (c) and 8 (d); i.e. from the FCC region between lamellar B2 plates and one of the ASL-intersected irregular B2, respectively. TEM results from both sites are presented in Figs. 9–11. Fig. 9 (a)

shows a bright field TEM (BFTEM) of the FCC region between two B2 (inset of Fig. 9 (a)). The microstructure contained both coarse and elongated features, which appeared to be subgrain boundaries. To confirm their presence, a SADP along [011]_{fcc} was recorded from a region marked with a circle in Fig. 9 (a). A close examination of the SADP presented in Fig. 9 (b) indicated a doublet of FCC reciprocal lattice reflections, which is marked with an arrow and is highlighted as an inset in Fig. 9 (b). This doublet was mutually separated by an azimuthal angle of ~4° with respect to the transmitted beam (marked as “0” in the SADP). Such small separation of reciprocal lattice reflections was indicative of subgrain [43], and suggested that the SADP was recorded from a region containing low-angle subgrain boundaries [43]. Further evidence of the subgrain boundaries can also be seen in the BFTEM (marked with arrows in Fig. 9 (a)), where some of the boundaries exhibited Moiré fringes (yellow-colored arrows) [43]. Note that the absence of superlattice reflections from the L1₂ phase (e.g. Fig. 1 (b) and 1 (c) from the as-cast microstructure) from the [011]_{fcc} SADP in Fig. 9 (a) suggested that the L1₂ phase may have been completely sheared or dissolved during the propagation of ASL; and, consequently, the L1₂ phase has, at least for the as-cast microstructure, minimal impact on strain localization. Nano-scale twins of thickness ~3–4 nm

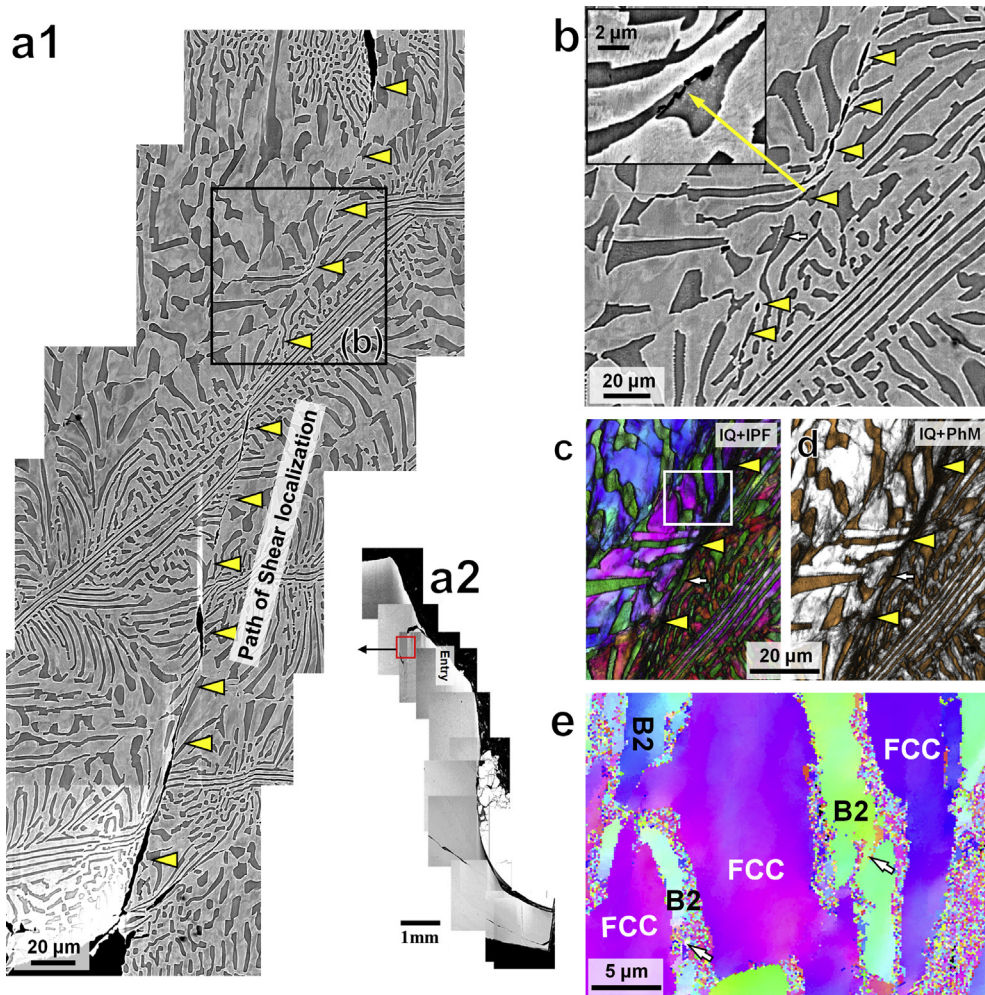


Fig. 7. Deformation features in the plugged specimen near the projectile entry point. (a1) Collage of BSE images showing ASL path marked with yellow colored arrows. Inset (a2) shows the location of the ASL near specimen edge. (b) Higher magnification BSE of the ASL (chosen from the box in (a)). Inset shows crack within an irregular B2 domain. EBSD of (b) showing (c) phase map, and (d) IPF. (e) High resolution EBSD of the region boxed in (d). (For interpretation of the references to color in this figure legend, the reader is referred to the Web version of this article.)

were also observed within the elongated subgrain. The presence of twins is also confirmed from their reflections in the $[011]_{\text{FCC}}$ SADP (bold rectangles in Fig. 9 (b)), and a corresponding dark field showing a twin variant (Fig. 9 (c)). More importantly, the deformed FCC regions exhibited strong signature of dynamic recovery (akin to stage IV of deformation in FCC metals [44]) via the subgrain formation, and their elongated morphology in the BFTEM suggested continued deformation of those subgrains via deformation twinning. These results postulate that the effective plastic strains experienced by the FCC phase in EHEA, during ballistic loading with a spherical impactor, easily exceed those of normal uniaxial tests and are well within the realm of superplastic deformation — consistent with claims by Esquivel and Murr, (see Figure 22 in Ref. [30]).

In stark contrast to the lamellar regions, FCC regions near the irregular B2 grain indicated the presence of recrystallized FCC grains (arrows in Fig. 10 (a)), where the recrystallized grain diameters varied from ~ 20 – 100 nm. Further evidence of FCC recrystallization was obtained by recording a SADP from the FCC region (dotted circle in Fig. 10 (a)), which showed ring patterns and $\{111\}_{\text{FCC}}$ recrystallization texture. Note that the BFTEM and the ring pattern were recorded by orienting a region within B2 close to its $[011]_{\text{B}2}$ zone axis (top-right inset in Fig. 10 (a)). Since FCC/B2 showed a KS OR in the initial microstructure (Fig. 4), i.e. $<011>_{\text{B}2} // <111>_{\text{FCC}}$ and $\{111\}_{\text{B}2} // \{011\}_{\text{FCC}}$, such an OR may have “crystallographically biased” the

subsequent FCC recrystallization texture to $\{111\}_{\text{FCC}}$.

The TEM studies also permitted us to examine in detail ASL-induced deformation of B2. The high-angle dark-field scanning TEM (HAADF-STEM) presented in Fig. 10 (c) reveals the damage within B2 via a “band” of brighter contrast that extends from the upper left corner (from the FCC matrix) to the bottom right-hand corner; deep into the B2 region. In other words, the path for shear localization intersects FCC/B2 interface boundaries, which is mechanistically comparable to the deformation features seen in the plugged condition (Fig. 7 (b)). To better understand the effect of ASL on FCC/B2 KS interfaces, we conducted TEM tilting experiments in the same region. Fig. 11 (a) and 11 (b) show the BFTEM and the corresponding DFTEM from that region, respectively. DFTEM was recorded by selecting one of the $\{111\}_{\text{FCC}}$ reflections; consequently, the FCC regions appear in brighter contrast in Fig. 11 (b). In particular, the DFTEM in Fig. 11 (b) allowed us to trace the structure of the deformed KS interface, which appears to contain “B2 ligaments” protruding out into the FCC matrix (marked with white arrow heads) and interfacial steps of height ~ 10 nm (marked with yellow arrow heads). Our previous examination of undeformed FCC/B2 semicoherent KS interfaces had revealed the presence of interfacial steps, but they were approximately a few atomic planes high, i.e. ~ 0.2 – 0.4 nm [45]. Therefore, the larger step sizes in Fig. 11 (b) likely were caused via dislocation-KS interface interactions that produced offsets ~ 40 – 70 times that of FCC Burgers vector. Further evidence of such interactions

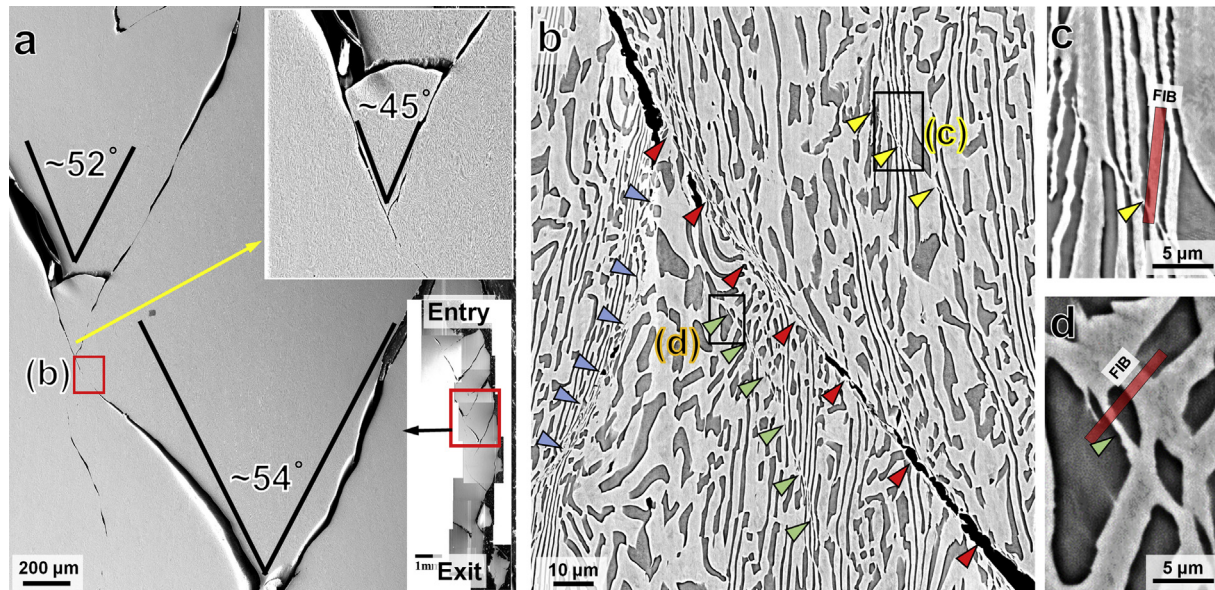


Fig. 8. Surface manifestation of damage in the completely penetrated specimen. (a) Low magnification image of two “V”-shaped cracks, while the top-right inset shows the angle formed at the intersection of two cracks. The bottom-right inset in “a” shows the location near the specimen edge. (b) Higher magnification image showing multiple ASL paths via blue, red, green and yellow colored arrows. Interaction of ASL path with (c) lamellar B2 and (d) clustered arrangements with irregularly shaped B2 domains. The transparent red boxes indicate the locations where FIB foils were extracted for TEM examination. (For interpretation of the references to color in this figure legend, the reader is referred to the Web version of this article.)

(Fig. 7 (c)) shows a pile-up of dislocations near an interfacial step. Similar deformation-induced step formation at the FCC/B2 interfaces had been reported earlier by Misra and Gibala using eutectic Ni-Al-Fe alloys [46]. They suggested that the interfacial steps caused residual dislocations at the interfaces due to slip-transfer mechanisms between FCC and B2 [46]. Additionally, near these steps, we also confirmed that some of the softer FCC phase also protruded into the B2 domain, which can be seen as brighter contrast regions inside B2 in Fig. 11 (b) and 11 (c) (indicated with white arrows). Thus, B2 domains experienced significant plastic deformation during ASL propagation, which is sufficient to cause minor intermixing of phase.

4. Discussion

The impact with spherical WC projectiles invariably had produced adiabatic shear localization (ASL) in all three conditions; i.e., partial penetration (Figs. 5 and 6), plugged (Fig. 7) and full penetration (8–11). The differing impact conditions also influenced the width of the bands formed via ASL propagation, i.e. adiabatic shear bands (ASBs); see Fig. 12. The ASB width were measured from the region marked with array of arrow-heads in Figs. 5, 7 and 8. We observe that, compared to the partially penetrated specimen, the ASB width increases by approximately two times in the plugged condition, and, within experimental scatter, retains the same width in the fully penetrated condition. In other words, the severity of impact, i.e. due to increase in projectile

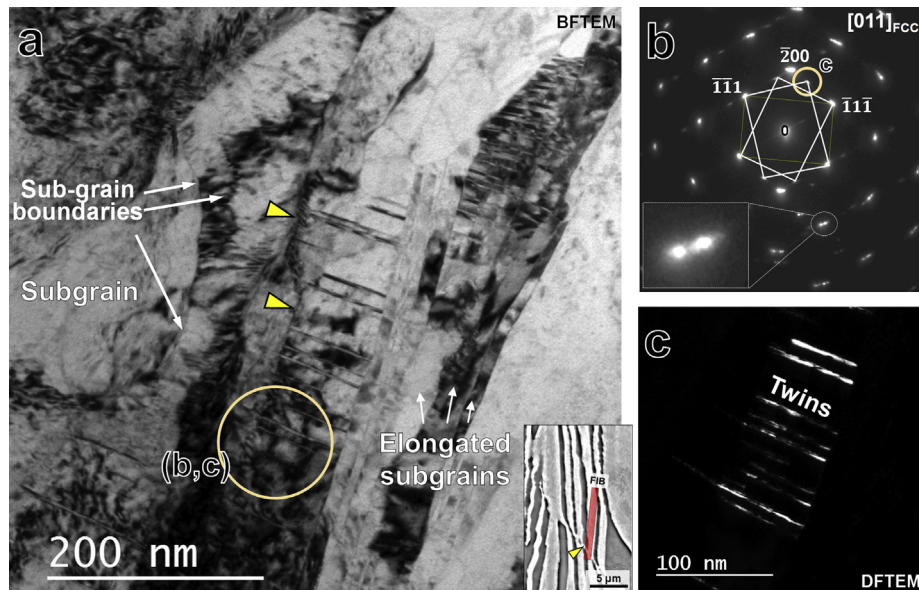


Fig. 9. TEM from the ASL within the lamellar B2 arrangements. (a) Representative bright-field TEM image showing sub-grain boundaries, elongated sub-grains and deformation twins within the sub-grains. (b) SADP from a region circled in (a) and (c) shows the DFTEM recorded from a twin reflection (circled in the SADP).

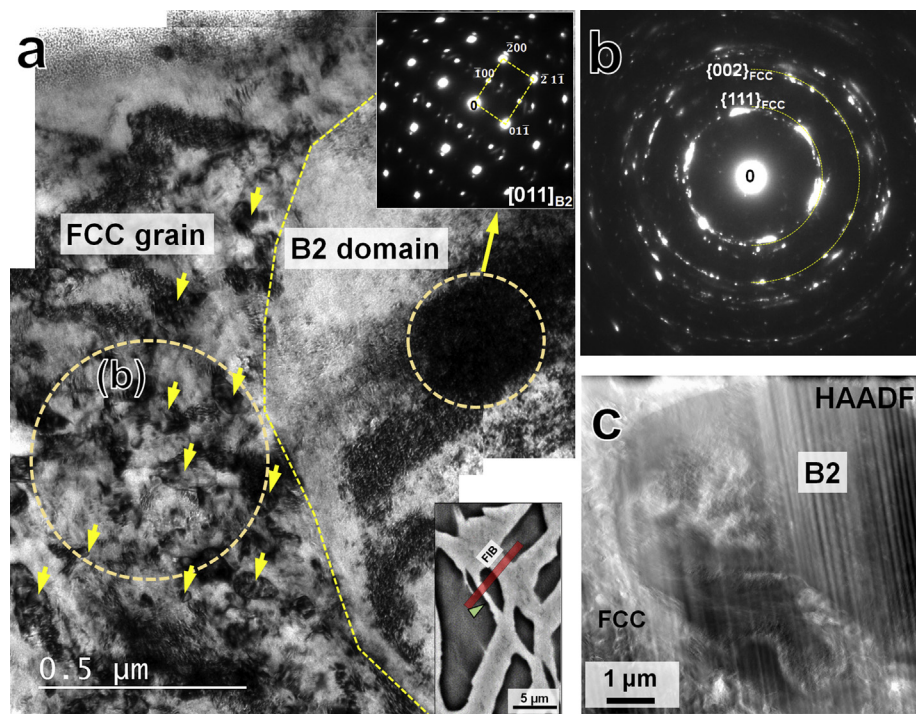


Fig. 10. TEM from the ASL within the clustered arrangements with irregularly-shaped B2 domains. (a) Collage of BFTEM showing the interfacial regions of B2 and the adjoining FCC region. Inset shows the [011] SAED recorded from B2 (smaller diameter circle in (a)). (b) SAED recorded from the FCC region in (a). (c) HAADF-STEM image of the region presented in the BFTEM in (a).

velocity, facilitates growth of ASL. Regardless, the formation and propagation of ASL was not hindered by the morphology of B2 domains, i.e. lamellar or irregularly-shaped clusters (see Figs. 1–4). Such morphology-independent ASL propagation is likely due to the 3D stress state of the deformation process, which caused ASL to form on the maximum shear planes; e.g. Fig. 8 (a). In other words, the microstructure behaves like a continuum with respect to ASL formation and propagation, with minimal influence from pre-existing microstructural heterogeneities like FCC/B2 interfaces (dominant feature) and fine-scale Cr-rich (within B2) and L1₂ (within FCC) precipitates.

However, substantial differences were noted in the location of cracks in the three conditions; and, in certain cases, correlations between the as-cast microstructure and the crack path could be extracted. After impact with lower projectile velocities, i.e. partial penetration, the cracks formed primarily along the Kurdjumov-Sachs interfaces of the lamellar B2 (Fig. 6). Examination of these regions using EBSD indicated that the adjoining FCC and B2 phases experienced mutual lattice movement/rotations. For example, Fig. 6 (d) shows that the

neighboring FCC and B2 had acquired a common crystallographic orientation that did not exist in the as-cast microstructure. These observations indicate that KS interface itself may have undergone movement or sliding. Such interfacial movement is plausible because FCC/BCC semicoherent interfaces are known to contain interfacial dislocations [47], which may have facilitated the relative movement between FCC and B2 phases at the interface. In contrast to the partially penetrated condition, the cracks in the plugged and fully-penetrated conditions formed along the ASL propagation path (Figs. 7 and 8). The suspicion is that the interfacial steps, caused by dislocation-KS interface interactions (Fig. 11 (c)), may have facilitated crack propagation across the FCC/B2 interfaces. Collectively, our results indicated that the formation and propagation of cracks in EHEAs are closely related to the structure of these FCC-B2 KS interfaces. Studies are underway to understand the atomic structure of these interfaces and their influence on dislocation plasticity of EHEAs. It appears that the differences in the ASB width seen in the partial and plugged/fully penetrated conditions, Fig. 12, may be related to the damage mechanisms observed in the

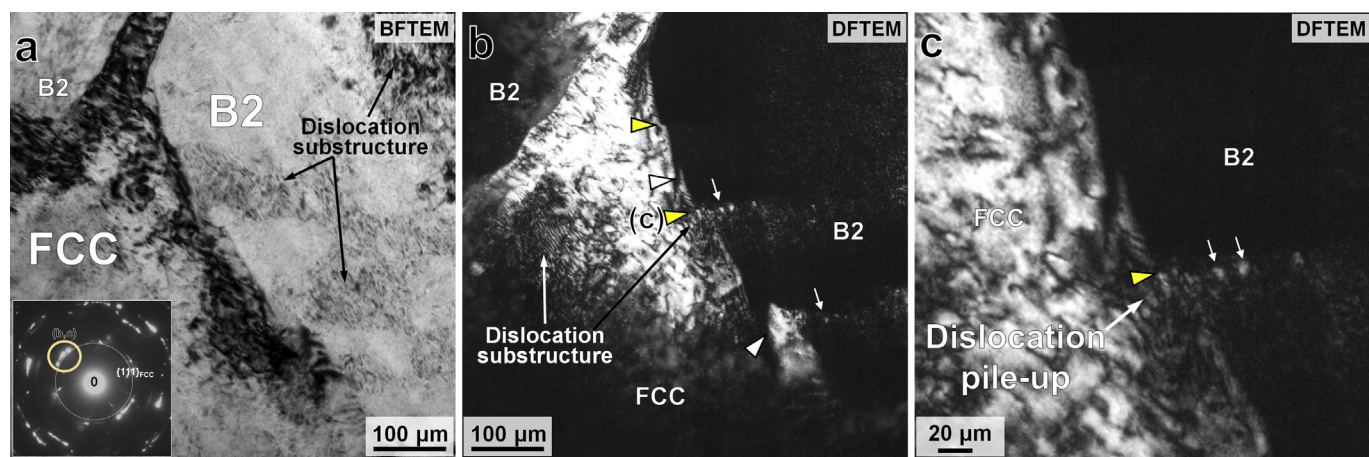


Fig. 11. TEM of deformation features near a FCC/B2 interface. (a) BFTEM showing the FCC/B2 region along with the SADP, (b) corresponding DFTEM showing deformation-induced step formation at FCC/B2 interfaces and “B2 ligaments”(marked with arrow heads), and (c) a higher magnification DFTEM showing dislocation pile-up near an interfacial step.

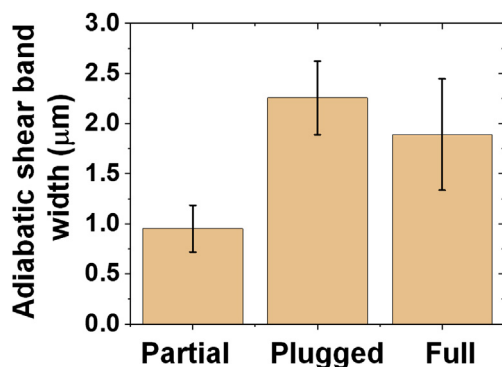


Fig. 12. Comparison of measured adiabatic shear band widths in the three impact conditions.

three conditions.

Regarding the effect of fine-scale precipitates in the as-cast microstructure (Figs. 1 (f) and 2) — L₁₂ precipitation appears to have minimal influence on crack propagation in FCC, while the Cr-rich precipitates noticeably deflect the crack path within B2. However, such crack deflection is observed only in case of larger irregularly-shaped B2 domains (compare Fig. 7 (b) and site “1” in Fig. 6 (a)). TEM examination of an ASL within FCC, in the fully penetrated condition, revealed that the FCC regions experience conditions comparable to high-temperature deformation, i.e., elongated subgrain formation and dynamic recrystallization (Fig. 9). Under such high-temperature deformation conditions, the L₁₂ phase either had been sheared by avalanche of dislocations within the propagating ASL, or may have simply dissolved because the temperatures reached the L₁₂ solvus limit. Possibly, particularly in the fully-penetrated condition, the combination of both factors may have rendered the L₁₂ precipitates ineffective.

5. Summary

We have attempted to correlate the initial as-cast microstructure of a AlCoCrFeNi_{2.1} EHEA with damage mechanisms prevalent during dynamic loading. Such loading was carried out by impact of ~0.5 inch AlCoCrFeNi_{2.1} plates with WC spheres at three different velocities — 0.803, 1.159 and 1.388 Km/s. Based on penetration depth, the ballistically-tested specimens were categorized as partially penetrated, plugged, and full or completely penetrated. SEM, EBSD and TEM were used to characterize the as-cast microstructure and to identify the damage mechanisms in the three ballistically-tested conditions. This detailed characterization of the pre- and post-deformed conditions yielded the following findings:

1. The as-cast AlCoCrFeNi_{2.1} microstructure is comprised primarily of FCC and bcc-ordered B2 phases. The B2 morphology varied from lamellar plates to irregularly-shaped clusters. Irrespective of morphology, the B2 domains exhibited primarily a Kurdjumov-Sachs orientation relationship with the FCC phase. The FCC and B2 phases also contained fine-scale FCC-ordered L₁₂ and Cr-rich precipitates, respectively.
2. Damage from dynamic or ballistic loading was manifested via adiabatic shear localization (ASL) and subsequent crack formation. ASL in the FCC phase was manifested as elongated subgrain formation, nanoscale twinning inside the subgrains, and dynamic recrystallization. While B2 accommodated ASL formation via extensive dislocation plasticity, such shear localization was observed in all three loading conditions and was independent of microstructural features.
3. However, the FCC/B2 interfaces appear to have a strong influence on crack formation. In the partially penetrated condition (i.e. impact at lower velocities) the cracks formed primarily along the FCC/B2 interfaces. On the other hand, cracks appear to trace the prior ASL path and cut through the FCC/B2 interfaces in the plugged and fully penetrated conditions, i.e., at higher velocities. Steps formed at the FCC/B2 interface, because dislocation KS boundary interactions may have facilitated such crack growth at higher velocities.
4. The L₁₂ precipitates had minimal influence on shear localization and crack propagation. However, the Cr-rich precipitates inside B2 domains appeared to deflect the crack path.

lamellar-B2 interfaces. On the other hand, cracks appear to trace the prior ASL path and cut through the FCC/B2 interfaces in the plugged and fully penetrated conditions, i.e., at higher velocities. Steps formed at the FCC/B2 interface, because dislocation KS boundary interactions may have facilitated such crack growth at higher velocities.

4. The L₁₂ precipitates had minimal influence on shear localization and crack propagation. However, the Cr-rich precipitates inside B2 domains appeared to deflect the crack path.

Declaration of competing interest

The authors have no conflict of interest.

Acknowledgments

The work was performed under a cooperative agreement between the U.S. Army Research Laboratory and the University of North Texas (W911NF-18-2-0067). We also acknowledge the Materials Research Facility at UNT for the microscopy facilities.

References

- [1] Yong Zhang, Ting Ting Zuo, Zhi Tang, Michael C. Gao, Karin A. Dahmen, Peter K. Liaw, Zhao Ping Lu, Microstructures and properties of high-entropy alloys, *Prog. Mater. Sci.* 61 (2014) 1–93.
- [2] Ming-Hung Tsai, Jian-Wei Yeh, High-entropy alloys: a critical review, *Mater. Res. Lett.* 2 (3) (2014) 107–123.
- [3] E.J. Pickering, N.G. Jones, High-entropy alloys: a critical assessment of their founding principles and future prospects, *Int. Mater. Rev.* 61 (3) (2016) 183–202.
- [4] Daniel B. Miracle, Oleg N. Senkov, A critical review of high entropy alloys and related concepts, *Acta Mater.* 122 (2017) 448–511.
- [5] Stéphane Gorsse, Daniel B. Miracle, Oleg N. Senkov, Mapping the world of complex concentrated alloys, *Acta Mater.* 135 (2017) 177–187.
- [6] Daniel Miracle, Bhaskar Majumdar, Katalin Wertz, Stéphane Gorsse, New strategies and tools to accelerate discovery and development of multi-principal element structural alloys, *Scr. Mater.* 127 (2017) 195–200.
- [7] G. Laplanche, P. Gaudau, O. Horst, F. Otto, G. Eggeler, E.P. George, Temperature dependencies of the elastic moduli and thermal expansion coefficient of an equiatomic, single-phase CoCrFeMnNi high-entropy alloy, *J. Alloy. Comp.* 623 (2015) 348–353.
- [8] G. Laplanche, O. Horst, F. Otto, G. Eggeler, E.P. George, Microstructural evolution of a CoCrFeMnNi high-entropy alloy after swaging and annealing, *J. Alloy. Comp.* 647 (2015) 548–557.
- [9] Deep Choudhuri, Bharat Gwalani, Stephane Gorsse, Mageshwari Komarasamy, Srinivas A. Mantri, Srivilliputhur G. Srinivasan, Rajiv S. Mishra, Rajarshi Banerjee, Enhancing strength and strain hardenability via deformation twinning in fcc-based high entropy alloys reinforced with intermetallic compounds, *Acta Mater.* 165 (2019) 420–430.
- [10] Bharat Gwalani, Stephane Gorsse, Deep Choudhuri, Yufeng Zheng, Rajiv S. Mishra, Rajarshi Banerjee, Tensile yield strength of a single bulk Al_{0.3}CoCrFeNi high entropy alloy can be tuned from 160 MPa to 1800 MPa, *Scr. Mater.* 162 (2019) 18–23.
- [11] B. Gwalani, D. Choudhuri, V. Soni, Y. Ren, M. Styles, J.Y. Hwang, S.J. Nam, H. Ryu, Soon Hyung Hong, R. Banerjee, Cu assisted stabilization and nucleation of L₁₂ precipitates in Al_{0.3}Cu_{0.7}Cr_{0.2}Ni₂ fcc-based high entropy alloy, *Acta Mater.* 129 (2017) 170–182.
- [12] Bharat Gwalani, Stephane Gorsse, Deep Choudhuri, Mark Styles, Yufeng Zheng, Rajiv S. Mishra, Rajarshi Banerjee, Modifying transformation pathways in high entropy alloys or complex concentrated alloys via thermo-mechanical processing, *Acta Mater.* 153 (2018) 169–185.
- [13] Yifeng Liao, Ian Baker, Microstructure and room-temperature mechanical properties of Fe₃₀Ni₂₀Mn₃₅Al₅, *Mater. Char.* 59 (11) (2008) 1546–1549.
- [14] Yifeng Liao, Ian Baker, On the room-temperature deformation mechanisms of lamellar-structured Fe₃₀Ni₂₀Mn₃₅Al₅, *Mater. Sci. Eng. A* 528 (12) (2011) 3998–4008.
- [15] Yifeng Liao, Ian Baker, Evolution of the microstructure and mechanical properties of eutectic Fe₃₀Ni₂₀Mn₃₅Al₅, *J. Mater. Sci.* 46 (7) (2011) 2009–2017.
- [16] Adenike M. Giwa, Peter K. Liaw, Karin A. Dahmen, Julia R. Greer, Microstructure and small-scale size effects in plasticity of individual phases of Al_{0.7}CoCrFeNi high entropy alloy, *Extreme Mech. Lett.* 8 (2016) 220–228.
- [17] Indranil Basu, Václav Ocelík, Jeff Th M. De Hosson, Size dependent plasticity and damage response in multiphase body centered cubic high entropy alloys, *Acta Mater.* 150 (2018) 104–116.
- [18] Indranil Basu, Václav Ocelík, Jeff Th M. De Hosson, BCC-FCC interfacial effects on plasticity and strengthening mechanisms in high entropy alloys, *Acta Mater.* 157 (2018) 83–95.
- [19] Sindhu Gangireddy, Bharat Gwalani, Vishal Soni, Rajarshi Banerjee, Rajiv S. Mishra, Contrasting mechanical behavior in precipitation hardenable Al_xCoCrFeNi high entropy alloy microstructures: single phase FCC vs. dual phase

- FCC-BCC, Mater. Sci. Eng. A 739 (2019) 158–166.
- [20] Bharat Gwalani, Sindhura Gangireddy, Yufeng Zheng, Vishal Soni, Rajiv S. Mishra, Rajarshi Banerjee, Influence of ordered L1₂ precipitation on strain-rate dependent mechanical behavior in a eutectic high entropy alloy, Sci. Rep. 9 (1) (2019) 6371.
- [21] Yiping Lu, Yong Dong, Sheng Guo, Li Jiang, Huijun Kang, Tongmin Wang, Bin Wen, et al., A promising new class of high-temperature alloys: eutectic high-entropy alloys, Sci. Rep. 4 (2014) 6200.
- [22] Yiping Lu, Xuzhou Gao, Li Jiang, Zongning Chen, Tongmin Wang, Jinchuan Jie, Huijun Kang, et al., Directly cast bulk eutectic and near-eutectic high entropy alloys with balanced strength and ductility in a wide temperature range, Acta Mater. 124 (2017) 143–150.
- [23] I.S. Wani, T. Bhattacharjee, S. Sheikh, Y.P. Lu, Subhradeep Chatterjee, Pinaki Prasad Bhattacharjee, S. Guo, N. Tsuji, Ultrafine-grained Al_{CoCrFeNi}_{2.1} eutectic high-entropy alloy, Mater. Res. Lett. 4 (3) (2016) 174–179.
- [24] I.S. Wani, T. Bhattacharjee, S. Sheikh, Pinaki Prasad Bhattacharjee, S. Guo, N. Tsuji, Tailoring nanostructures and mechanical properties of Al_{CoCrFeNi}_{2.1} eutectic high entropy alloy using thermo-mechanical processing, Mater. Sci. Eng. A 675 (2016) 99–109.
- [25] I.S. Wani, T. Bhattacharjee, S. Sheikh, Y. Lu, S. Chatterjee, S. Guo, Pinaki Prasad Bhattacharjee, N. Tsuji, Effect of severe cold-rolling and annealing on microstructure and mechanical properties of Al_{CoCrFeNi}_{2.1} eutectic high entropy alloy, In IOP Conference Series: Materials Science and Engineering, vol. 194, IOP Publishing, 20170120181.
- [26] I.S. Wani, T. Bhattacharjee, S. Sheikh, I.T. Clark, M.H. Park, T. Okawa, S. Guo, Pinaki Prasad Bhattacharjee, N. Tsuji, Cold-rolling and recrystallization textures of a nano-lamellar Al_{CoCrFeNi}_{2.1} eutectic high entropy alloy, Intermetallics 84 (2017) 42–51.
- [27] Tianhao Wang, Mageshwari Komarasamy, Shivakant Shukla, Rajiv S. Mishra, Simultaneous enhancement of strength and ductility in an Al_{CoCrFeNi}_{2.1} eutectic high-entropy alloy via friction stir processing, J. Alloy. Comp. 766 (2018) 312–317.
- [28] Xuzhou Gao, Yiping Lu, Bo Zhang, Ningning Liang, Guanzhong Wu, Gang Sha, Jizi Liu, Yonghai Zhao, Microstructural origins of high strength and high ductility in an Al_{CoCrFeNi}_{2.1} eutectic high-entropy alloy, Acta Mater. 141 (2017) 59–66.
- [29] Shivakant Shukla, Tianhao Wang, Shomari Cotton, Rajiv S. Mishra, Hierarchical microstructure for improved fatigue properties in a eutectic high entropy alloy, Scr. Mater. 156 (2018) 105–109.
- [30] E.V. Esquivel, L.E. Murr, Deformation effects in shocked metals and alloys, Mater. Sci. Technol. 22 (4) (2006) 438–452.
- [31] Marc A. Meyers, Dynamic Behavior of Materials, John Wiley & Sons, 1994.
- [32] Bradley Dodd, Yilong Bai (Eds.), Adiabatic Shear Localization: Frontiers and Advances, Elsevier, 2012.
- [33] Deep Choudhuri, Philip A. Jannotti, Saideep Muskeri, Shivakant Shukla, Sindhura Gangireddy, Sundeep Mukherjee, Brian E. Schuster, Jeffrey T. Lloyd and Rajiv S. Mishra, — manuscript in submission.
- [34] Deep Choudhuri, Srinivas Aditya Mantri, Talukder Alam, Srikumar Banerjee, Rajarshi Banerjee, Precipitate-dislocation interaction mediated Portevin-Le Chatelier-like effect in a beta-stabilized Ti-Mo-Nb-Al alloy, Scr. Mater. 124 (2016) 15–20.
- [35] T. Borkar, B. Gwalani, D. Choudhuri, T. Alam, A.S. Mantri, M.A. Gibson, R. Banerjee, Hierarchical multi-scale microstructural evolution in an as-cast Al₂CuCrFeNi₂ complex concentrated alloy, Intermetallics 71 (2016) 31–42.
- [36] Deep Choudhuri, Shivakant Shukla, Abhinav Jagetia and Rajiv S. Mishra, — manuscript in preparation.
- [37] N. Kumar, Q. Ying, X. Nie, R.S. Mishra, Z. Tang, P.K. Liaw, R.E. Brennan, K.J. Doherty, K.C. Cho, High strain-rate compressive deformation behavior of the Al_{0.1}CrFeCoNi high entropy alloy, Mater. Des. 86 (2015) 598–602.
- [38] Sindhura Gangireddy, Kaimiao Liu, Bharat Gwalani, Rajiv Mishra, Microstructural dependence of strain rate sensitivity in thermomechanically processed Al_{0.1}CoCrFeNi high entropy alloy, Mater. Sci. Eng. A 727 (2018) 148–159.
- [39] Frederik Otto, A. Dlouhý, Ch Somsen, Hongbin Bei, G. Eggeler, Easo P. George, The influences of temperature and microstructure on the tensile properties of a CoCrFeMnNi high-entropy alloy, Acta Mater. 61 (2013) 5743–5755.
- [40] D. Choudhuri, M. Komarasamy, V. Ageh, R.S. Mishra, Nvestigation of plastic deformation modes in Al0.1CoCrFeNi high entropy alloy, Mater. Chem. Phys. 217 (2018) 308–314.
- [41] F. Martinez, L.E. Murr, A. Ramirez, M.I. Lopez, S.M. Gaytan, Dynamic deformation and adiabatic shear microstructures associated with ballistic plug formation and fracture in Ti-6Al-4V targets, Mater. Sci. Eng. A 454 (2007) 581–589.
- [42] L.E. Murr, A.C. Ramirez, S.M. Gaytan, M.I. Lopez, E.Y. Martinez, D.H. Hernandez, E. Martinez, Microstructure evolution associated with adiabatic shear bands and shear band failure in ballistic plug formation in Ti-6Al-4V targets, Mater. Sci. Eng. A 516 (2009) 205–216.
- [43] David B. Williams, C. Barry Carter, "The Transmission Electron microscope." in Transmission Electron Microscopy, Springer, Boston, MA, 1996, pp. 3–17.
- [44] U.F. Kocks, H. Mecking, Physics and phenomenology of strain hardening: the FCC case, Prog. Mater. Sci. 48 (3) (2003) 171–273.
- [45] Deep Choudhuri, Shivakant Shukla, Bharat Gwalani, Rajarshi Banerjee, S. Rajiv, Mishra, Deformation induced intermediate metastable lattice structures facilitate ordered B2 nucleation in a fcc-based high entropy alloy, Mater. Res. Lett. 7 (1) (2019) 40–46.
- [46] A. Misra, R. Gibala, Slip transfer and dislocation nucleation processes in multiphase ordered Ni-Fe-Al alloys, Metall. Mater. Trans. A 30 (4) (1999) 991–1001.
- [47] J.H. Van der Merwe, G.J. Shiflet, The role of structural ledges at phase boundaries- III. FCC-BCC interfaces in Kurdjumov-Sachs orientation, Acta Metall. Mater. 42 (1994) 1199–1205.